



Constructing core-shell carbon fiber/polypyrrole/CoFe₂O₄ nanocomposite with optimized conductive loss and polarization loss toward efficient electromagnetic absorption

Liyang Yuan¹ · Wenxin Zhao¹ · Yukun Miao¹ · Chang Wang¹ · Anguo Cui² · Zhongning Tian¹ · Ting Wang³ · Alan Meng³ · Meng Zhang¹ · Zhenjiang Li¹

Received: 17 October 2023 / Revised: 21 February 2024 / Accepted: 23 February 2024 / Published online: 6 April 2024
© The Author(s), under exclusive licence to Springer Nature Switzerland AG 2024

Abstract

The inadequate impedance matching and weak attenuation capability for incident electromagnetic waves exhibited by carbon fibers (CF) are critical factors limiting their application served as absorbing materials. Constructing a nanocomposite system that simultaneously exhibits both dielectric loss and magnetic loss characteristics is a feasible strategy to overcome these limitations. In the present study, a core-shell CF@PPy@CoFe₂O₄ nanocomposite is fabricated through electrodeposition and subsequent hydrothermal methods to enhance the attenuation capacity and impedance matching of bare CF. Under the synergistic effects of diverse components and a peculiar network structure, the nanocomposite demonstrates optimized conductive loss and polarization loss, which results in a remarkable electromagnetic wave absorption performance with a minimum reflection loss (RL_{min}) of -55.33 dB and an effective absorption bandwidth (EAB) of 6.48 GHz (12 ~ 18 GHz) at optimal thicknesses of 2.11 and 2.42 mm, respectively, suggesting its promising application as a candidate absorber. More importantly, the exploration concerning the absorption mechanism provides significant insights into the attenuation modes of the dielectric-magnetic loss hetero-junction, which is beneficial for developing similar absorbing materials.

Keywords Conductive loss · Polarization loss · Electromagnetic absorption · The absorption mechanism · Dielectric-magnetic loss hetero-junction · The synergistic effects

✉ Meng Zhang
mengzhang@qust.edu.cn

✉ Zhenjiang Li
zhenjiangli@qust.edu.cn

¹ College of Materials Science and Engineering, Qingdao University of Science and Technology, Qingdao, Shandong province 266042, China

² College of Electromechanical Engineering, Qingdao University of Science and Technology, Qingdao, Shandong province 266061, China

³ College of Chemical Engineering, Key Laboratory of Optic-electric Sensing and Analytical Chemistry for Life Science, Shandong Key Laboratory of Biochemical Analysis, College of Chemistry and Molecular Engineering, MOE, Qingdao University of Science and Technology, Qingdao, Shandong province 266042, China

1 Introduction

Over the last decade, a variety of electronic devices that use electromagnetic wave as a medium have been extensively deployed in various domains, including telecommunications, aerospace, and automobiles [1]. However, the widespread presence of these electronic products has heightened public concerns about electromagnetic radiation pollution and potential health risks [2, 3]. To mitigate these issues, electromagnetic wave absorbing materials, which possess the capability to effectively dissipate electromagnetic wave and convert it into other energy forms, have increasingly captured the attention of researchers [4, 5].

Currently, due to their high electrical conductivity, excellent chemical stability, tunable dielectric properties, cost-effectiveness, and wide availability of raw materials, carbon-based materials (such as carbon nanotubes, porous carbon, graphene, and carbon fibers, etc.) have emerged as the preferred choice for producing electromagnetic wave absorbers

[6]. Undoubtedly, carbon fiber (CF) [7], serving as a outstanding reinforcing material, has exhibited exceptional performance in the realm of high-strength structural composites [8, 9]. As the concept of integrated structure and function in carbon fiber materials gradually takes root, research into their novel functional characteristics becomes increasingly pressing. This exploration is beneficial for expanding their application range and meeting the practical requirements of electromagnetic protection in various future industries [10].

It is widely acknowledged that a single carbon component struggles to achieve optimal impedance matching conditions [11]. Moreover, the simplistic mechanism by which CF interacts with incident electromagnetic wave often results in unsatisfactory attenuation effects. Constructing CF-based composite is a feasible and frequently utilized strategy, often employed by numerous researchers to enhance the electromagnetic wave absorption performance of individual CF [12]. Wang et al. [13] successfully developed flexible CF@ZnO composites, which achieve an effective absorption bandwidth (EAB) of 10.6 GHz, covering both the whole X and Ku bands. In another study, Wang and colleagues [14] fabricated a CF@MXene@MoS₂ nanocomposite with a three-dimensional layered structure, and the product achieves a minimum reflection loss (RL_{min}) of -61.51 dB at a matching thickness of 3.5 mm, while demonstrating an EAB value of 7.6 GHz at 2.1 mm. Zhang et al. [15] investigated the wave absorption performance of the CF@MoS₂ composite, which exhibited an EAB value of 10.85 GHz at a matching thickness of 3.8 mm. These research achievements have not only contributed significantly towards constructing CF-based composite absorbing materials, but also highlighted the tremendous application potential as effective electromagnetic wave absorbers. However, the pursuit of superior absorption performance at thinner matching thickness inspires ongoing research in this field.

Conductive polymers [16], represented by polyurethane, polypyrrole, and polythiophene, fall under the category of dielectric loss type absorbing materials, which also exhibits remarkable compatibility with CF [17]. The composite made of CF and conductive polymer retains the native conductive loss of CF. It also enhances the interface loss capability when encountering incident electromagnetic wave, achieving superior absorption performance compared to CF alone. On the other hand, the magnetic components based on iron, cobalt, nickel can generate strong magnetic loss against incident electromagnetic wave. By compounding them with dielectric loss components, it ensures that the composite material obtains more appropriate impedance matching condition and improved electromagnetic wave attenuation performance. However, when relying solely on dielectric loss and interface polarization, these composites struggle to effectively attenuate incident electromagnetic wave [18]. Moreover, the impedance matching has not yet

reached optimal condition, resulting in that the EAB value, matching thickness, and RL_{min} cannot meet the requirements for “thinness, lightness, width, and strength” [19–21]. To address this issue, magnetic components are typically introduced into the absorbing material system [22]. While realizing the dual action of dielectric-magnetic losses [23], it further improves the impedance matching of the composites, thus achieving superior absorptive performance [24, 25]. Ding et al. [26] fabricated a core-shell nanomaterial (TiO₂@Fe₃O₄@PPy) via a sequential solvent heat treatment and polymerization process. By manipulating the thickness of the polypyrrole layer, the electromagnetic wave absorption properties can be regulated. This achieves a RL_{min} of -61.8 dB at a thickness of 3.2 mm and an EAB value of 6 GHz at an optimal thickness of 2.2 mm. Zhang and collaborators [27] successfully synthesized CF@PANI@Fe₃O₄ hybrid nanocomposite and also proposed a synergistic mechanism of multiple reflection/scattering, dipole polarization, interfacial polarization, eddy current, and magnetic resonance, thus demonstrating a multiple attenuation method of incident electromagnetic wave, and the RL_{min} of 46.86 dB was achieved at a matching thickness of 2.7 mm. Liu’s group [28] successfully synthesized structured Fe₃O₄@SiO₂@PPy microspheres using a microemulsion polymerization technique. The product demonstrated a RL_{min} of -40.9 dB at a matching thickness of 5 mm and an EAB value of approximately 6.88 GHz (11.12~18 GHz), which encapsulates the entire K-band (12~18 GHz).

In this paper, a nanocomposite electromagnetic wave absorber, CF@PPy@CoFe₂O₄, is developed by successively depositing a PPy layer and magnetic CoFe₂O₄ particles onto the CF surface using the electrodeposition and hydrothermal methods, respectively. The PPy layer enhances the impedance matching condition and dielectric loss capability, while the presence of CoFe₂O₄ nanoparticle provides magnetic loss capability to the bare CF, further amplifying its attenuation capability. Through the use of a large number of heterogeneous interfaces, the coaxial core-shell structures generate robust interfacial polarization, meanwhile, the structural defects and adsorbed functional groups produce dipole polarization, owing to the synergistic effect of these multiple loss mechanisms, the CF@PPy@CoFe₂O₄ nanocomposite exhibits optimal impedance matching and excellent attenuation capabilities.

2 Experimental methods

2.1 Materials and chemicals

The CF substrate used in this study was provided by Shanghai Huayu Instrument Co., Ltd. Various chemical reagents, including hydrochloric acid (HCl), sodium chloride (NaCl),

iron chloride hexahydrate ($\text{FeCl}_3 \cdot 6\text{H}_2\text{O}$), cobalt chloride hexahydrate ($\text{CoCl}_2 \cdot 6\text{H}_2\text{O}$), and ethylene glycol (EG) were all purchased from Sinopharm Chemical Reagent Co., Ltd. Pyrrole ($\text{C}_4\text{H}_5\text{N}$) and anhydrous sodium acetate (CH_3COONa) were acquired from Aladdin Reagent. The pyrrole used was of analytical purity grade, whereas the other reagents were of chemical grade and did not require further purification.

2.2 Preparation process of CF@PPy nanocomposite

In this study, a CF@PPy composite was prepared by electrochemical deposition using CF as the substrate. Initially, the CF was segmented into 2 cm x 2 cm sections, then immersed in 1 mol/L hydrochloric acid for 3 h, followed by repeated rinsing with deionized water. In the electrochemical workstation setup, the CF served as the working electrode, a platinum plate electrode was employed as the counter electrode, and the $\text{Hg}/\text{Hg}_2\text{Cl}_2$ was used as reference electrode. The electrolyte was prepared with a pyrrole monomer concentration of 0.1 mol/L and a sodium chloride solution concentration of 1 mol/L. Cyclic voltammetry mode (CV) was conducted within a voltage window of 0~0.8 V at a scan rate of 10 mV/s. At a predetermined cycles number, the sample was rinsed with deionized water and dried at 60 °C to obtain the CF@PPy sample. By varying the number of cycles to 30, 60, 90, and 120, the corresponding resultant samples were labeled as CP-30, CP-60, CP-90, and CP-120, respectively.

The formation mechanism of PPy molecules can be summarized as follows: Firstly, under the influence of an electric field, pyrrole monomer molecules lose electrons at the surface of the electrode, resulting in the formation of cationic free radicals. Then, these pyrrole free radicals interact with another monomer to create a pyrrole dimer. Subsequently, an extensive PPy molecular chain is produced through a series of similar reactions.

2.3 Preparation of CF@PPy@CoFe₂O₄ nanocomposite

A solution was prepared by dissolving 5 mmol $\text{FeCl}_3 \cdot 6\text{H}_2\text{O}$ and 2.5 mmol $\text{CoCl}_2 \cdot 6\text{H}_2\text{O}$ in 70 mL ethylene glycol, followed by vigorous stirring for 30 min. Subsequently, 7.3 g anhydrous sodium acetate was added to the solution and stirred for an additional hour. The resulting mixture was then transferred into a reaction vessel, and the pre-determined CF@PPy sample was also introduced. The reaction was maintained at a temperature of 180 °C for a period of 8 h. The sample was subsequently rinsed with deionized water and dried at 60 °C to yield the CF@PPy@CoFe₂O₄ nanocomposite.

2.4 Characterization

The electrochemical deposition process was conducted using a CHI660E electrochemical workstation. The morphology of the

products was examined using scanning electron microscopy (SEM, Hitachi S-8400) and transmission electron microscopy (TEM, Hitachi H-8100), while their phase composition was investigated by a powder X-ray diffraction (XRD, Bruker D8) conducted at room temperature. Fourier infrared spectroscopy (FT-IR, Nicolet-6700) was used to analyze the functional groups of the products, and Raman spectroscopy (Renishaw 2000) was employed to evaluate the graphitization degree and defect content within the samples. The magnetization hysteresis loops of CF@PPy@CoFe₂O₄ hybrid nanomaterial was recorded using a vibrating sample magnetometer (VSM, Quantum Design, PPMS-9). X-ray photoelectron spectrometer (XPS, Thermo Scientific, ESCALAB 250XI) was used to detect the composition and chemical bonding state of the samples. The N₂ adsorption/desorption isotherm was determined by automatic specific surface and porosity analyzer (Micromeritics ASAP 2460), and the specific surface area of the sample was calculated by Brunauer-Emmett-Teller (BET) the model. Thermogravimetric analysis (TGA) of CF@PPy@CoFe₂O₄ nanocomposite was carried out in an argon atmosphere with a heating rate of 10 °C/min. The electromagnetic wave absorption performance of the samples was gauged by measuring electromagnetic parameters using a vector network analyzer (Agilent, N5230A) after compressing a ring with an internal diameter of 3.04 mm, an external diameter of 7.00 mm, and a thickness of 3.00 mm, which was mixed with epoxy resin under a packing load of 2 wt%.

3 Results and discussion

Figure 1a depicts a schematic representation of the synthesis process of CF@PPy@CoFe₂O₄ nanocomposite. The PPy shell was initially wrapped on the surface of CF via an electrodeposited process, resulting in the creation of CF@PPy nanocomposite. Subsequently, magnetic CoFe₂O₄ nanoparticles were integrated onto the nanocomposite using a straightforward hydrothermal method. To provide a more detailed understanding of the microscopic morphology, SEM was employed for characterization. Figure 1b displays a representative SEM image of a parallel CF sample with a diameter of approximately 8 μm. Notably, numerous subtle ditches aligned along the axis direction of CF provide a wealth of functional groups and active sites, which is beneficial for the subsequent growth of PPy shell. Figure 1c–f display typical SEM images of the CF@PPy nanocomposite, with the PPy shell densely coated on the CF surface, without disturbing the original orientation of the CF. Significantly, an increase in the nanocomposites diameter is observed in line with the number of electrodeposition cycles. Figure S1 provides cross-sectional SEM images of various CF@PPy nanocomposites. It can be clearly observed that the variation in the diameter of different nanocomposites can be clearly attributed to the

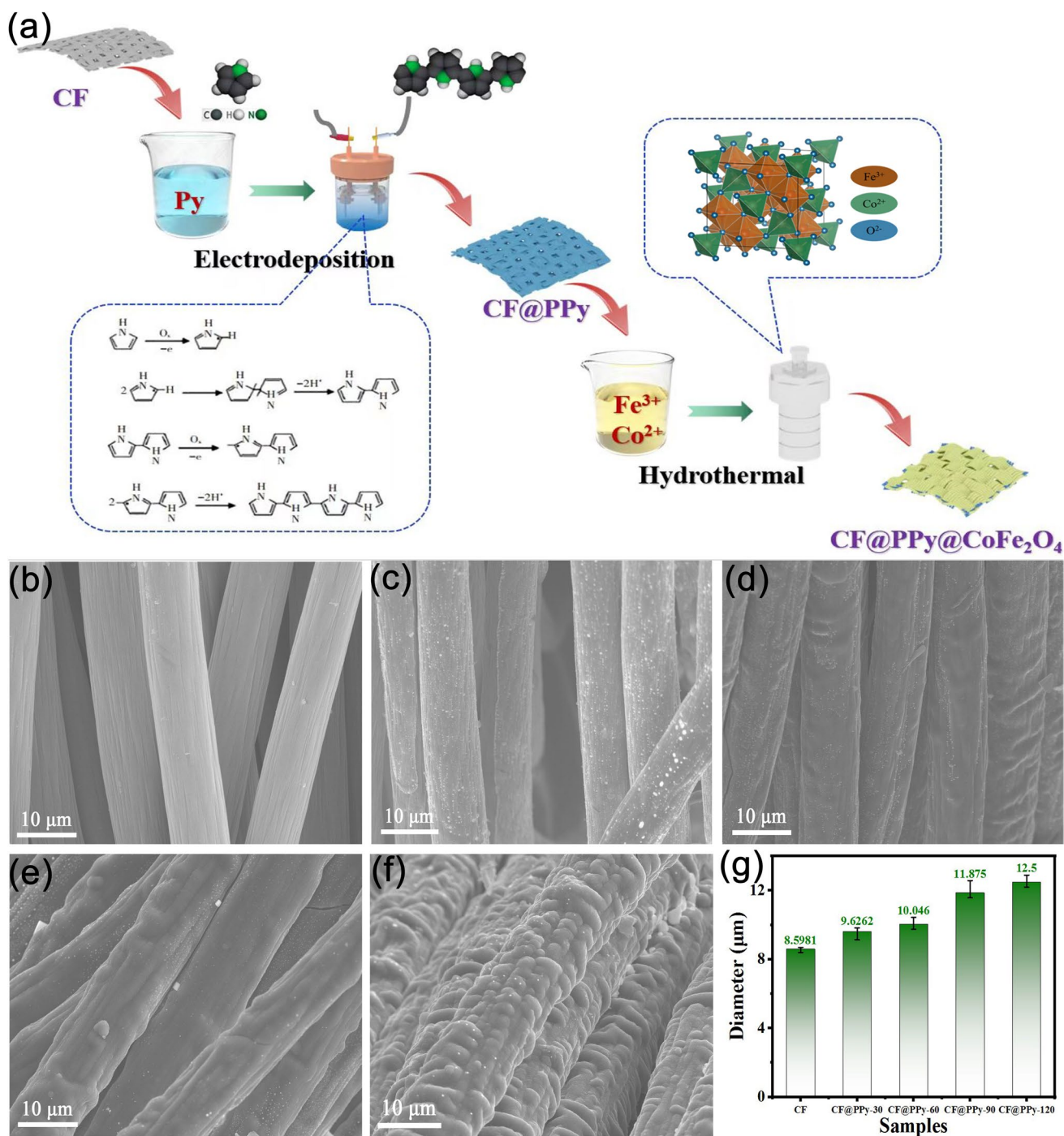


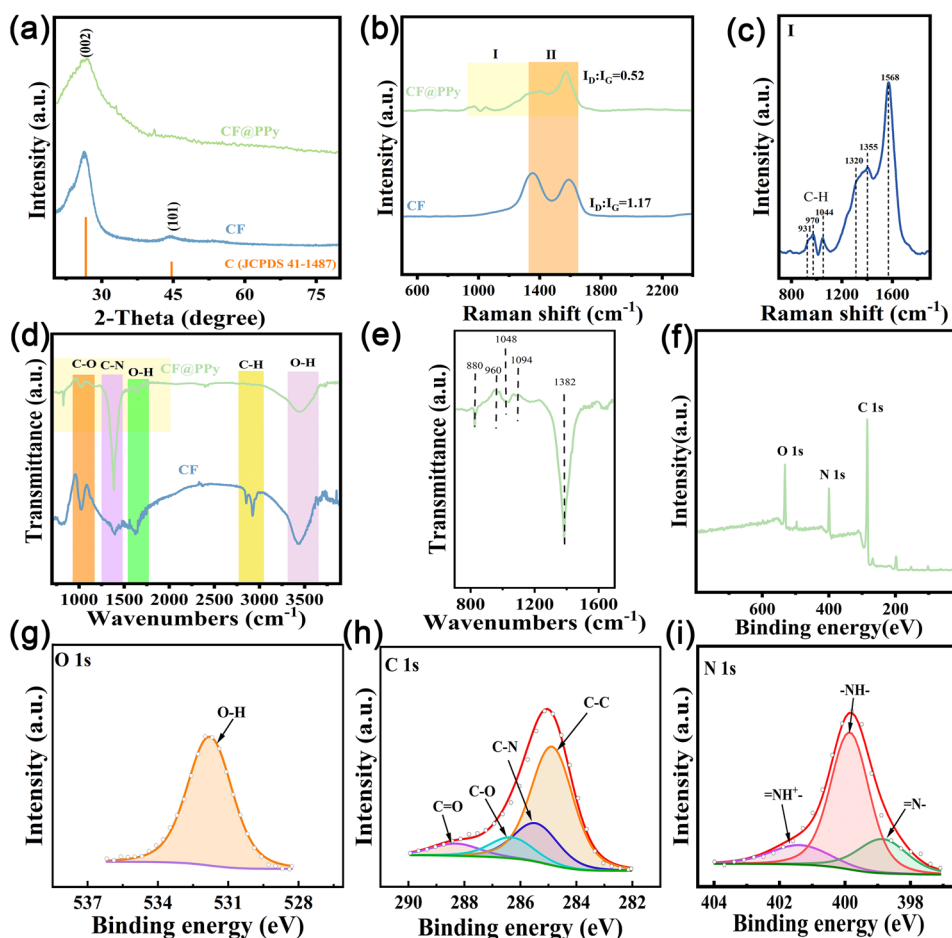
Fig. 1 a Schematic illustration of synthesis process of the CF@PPy@CoFe₂O₄ nanocomposite; SEM images of the b CF, c CP-30, d CP-60, e CP-90, f CP-120; g Comparison of the diameter values of the CF and the as-prepared CF@PPy samples

increasing thickness of the PPy shell, which correlates directly with the number of electrodeposition cycles. Furthermore, the PPy shell demonstrates an irregular profile, which potentially causes incident electromagnetic wave to undergo multiple reflections, thereby enhancing the attenuation characteristics of the nanocomposites. Crucially, an effective interface

is established between the CF and the PPy shell, fostering increased interfacial polarization and promoting the loss of incident electromagnetic waves at the interface.

The phase structure information of CF and CF@PPy samples was analyzed using XRD, with results displayed in Fig. 2a. The XRD patterns of the pure CF sample reveal

Fig. 2 **a** XRD patterns, **b** Raman spectra of the CF@PPy; **c** Raman localized magnification of CF@PPy; **d**, **e** FT-IR spectra of CF@PPy; High-resolution XPS spectra of CF@PPy **f** total spectrum; **g** O 1s; **h** C 1s; **i** N 1s



two broad diffraction peaks at approximately 25.8° and 44.6° , characteristic of disordered carbon. The diffraction peaks in the CF@PPy sample are notably less intense than in the CF, suggesting the formation of amorphous PPy. To better understand the microstructure of PPy on CF, Raman and FT-IR spectra were captured, as depicted in Fig. 2b–e. Figure 2b shows the Raman spectra of the two samples with characteristic PPy peaks delineated in the highlighted yellow box (Fig. 2c). The peaks at 931 cm^{-1} and 970 cm^{-1} correspond to the polarization and bipolarization properties of the quinone-type structure, while the peak near 1044 cm^{-1} can be assigned to the in-plane deformation of the C-H bonds [29]. Moreover, the peaks observed near 1355 cm^{-1} and 1568 cm^{-1} can be associated with the ring stretching of C=C bonds and the π -bonded conjugated structure of the polymer backbone [30, 31]. Both samples, due to the presence of carbon materials, exhibit two characteristic peaks around 1340 cm^{-1} and 1591 cm^{-1} , representing the D-band and G-band, respectively [32]. The D-band arises from the vibrations of defects in the disordered graphitic carbon and sp^3 hybridization, while the G-band is induced by the planar vibrations of sp^2 hybridized graphitic carbon within the carbocyclic ring system.

Generally, the relative intensity ratio (I_D/I_G) of the D and G bands is representative of the degree of graphitization or defects within the carbon material. In the given figure, the I_D/I_G values of the two materials are 1.17 and 0.52, respectively. The decrease in the I_D/I_G value of CF@PPy nanocomposite is mainly due to the incorporation of PPy, which results in a greater degree of π -bond conjugation within the polymer backbone [33]. This leads to an enhanced level of graphitization and a subsequent decrease in the I_D/I_G value [34].

Figure 2d shows the FT-IR spectra of the sample, with the sections enclosed in the boxes of varying colors representing the distinct peaks of the CF. The peaks located near 3646 cm^{-1} and 1664 cm^{-1} correspond to the O-H stretching vibration of the hydrogen bond, while the features located near 2912 cm^{-1} and 1021 cm^{-1} are attributed to the in-plane vibration of the -C-H bond [35]. The characteristic peak appearing near 1385 cm^{-1} is due to the C-O bending vibration. Some characteristic peaks of PPy can be observed in the locally zoomed-in image within the yellow box [36]. These encompass the stretching vibration of the C-N bond located near 1382 cm^{-1} , the intra-plane deformation vibration of the NH^+ detected near 1094 cm^{-1} , and the intra-plane

deformation vibration of the N-H bond as well as C-H bond (1048 cm^{-1}). The characteristic peaks positioned at 960 cm^{-1} and 880 cm^{-1} can be respectively ascribed to the ring out-of-plane deformation vibrations of the C-C bond and the ring out-of-plane deformation vibrations of the C-H bond.

XPS was employed to investigate the surface elemental valence states and chemical bonding configurations of CF@PPy. The comprehensive XPS spectrum of the CF@PPy sample (Fig. 2f) distinctly demonstrates the presence of C, N, and O elements. Compared with bare CF characterization results (Fig. S2) [37], the detection of N can be reasonably attributed to the introduction of PPy [38]. The energy spectrum of O1s (Fig. 2g) reveals a characteristic peak at a binding energy of 531.79 eV, correlating with the surface adsorption of water (OH-) [39]. The C1s energy spectrum of CF@PPy (Fig. 2h) can be deconvoluted into four splitting peaks, corresponding to C-C (284.8 eV), C-N (285.6 eV), C-O (286.3 eV), and C=O (288.2 eV) bonds. The emergence of C-N is most likely due to the existence of PPy [40]. Furthermore, the N1s energy spectrum (Fig. 2i) can be divided into three splitting peaks, indicating that the N atom primarily exists in the form of benzenemethanamine (-NH-), with a lesser amount present as quinoneimine (-N=) and a positively charged nitrogen atom (-NH⁺=) [41]. These findings further corroborate the successful introduction and encapsulation of PPy on the CF surface.

For evaluating the response characteristics of an absorber to electromagnetic waves, two factors are significant, relative complex permittivity ($\epsilon_r = \epsilon' - j\epsilon''$) and complex permeability ($\mu_r = \mu' - j\mu''$) [42]. These factors reflect the capability to store and dissipate electric field energy and magnetic field energy, and further determine the reflection coefficient and transmission coefficient of the absorber. Figure 3a–c depict the trends of ϵ' , ϵ'' , and $\tan\delta_\epsilon$ curves of both CF and CF@PPy nanocomposites within the frequency range of 2~18 GHz [43]. It is clearly evident from the figure that the CF@PPy nanocomposites exhibit superior values of ϵ' , ϵ'' , and $\tan\delta_\epsilon$ as compared to bare CF, signifying an enhanced dielectric loss capacity. Moreover, Fig. 3a demonstrates that with an increase in frequency, the curves tend to stabilize in the frequency range of 2~12 GHz, indicating a consistent capability of the absorber to store electrical energy. However, the ϵ' curves of all samples exhibit fluctuations within the range of 12~18 GHz, likely due to inherent defects. In the ϵ'' curve (Fig. 3b), multiple resonance peaks are observed in the CF@PPy samples, which can be attributed to the existence of numerous heterogeneous interfaces. These interfaces induce interfacial polarization, leading to the appearance of resonance peaks. The dielectric loss capability of an absorber is usually assessed by its dielectric loss tangent, calculated as

$\tan\delta_\epsilon = \epsilon''/\epsilon'$. As depicted in Fig. 3c, the CP-90 sample also exhibits elevated ϵ'' values and superior dielectric loss capability, suggesting that the complex permittivity of the sample can be effectively manipulated by adjusting the number of electrodeposition cycles, thereby optimizing its dielectric loss capability [44].

$$Z_{in} = Z_0 \sqrt{\frac{\mu_r}{\epsilon_r}} \tanh\left[j\left(\frac{2\pi fd}{c}\right)\sqrt{\mu_r \epsilon_r}\right] \quad (1)$$

$$RL(\text{dB}) = 20 \lg \left| \frac{Z_{in} - Z_0}{Z_{in} + Z_0} \right| \quad (2)$$

In above formula, the normalized input impedance is denoted as Z_{in} , while Z_0 represents the impedance in free space [45]. The complex permittivity and complex permeability are ϵ_r and μ_r , respectively. The frequency of the incident electromagnetic wave is denoted as f , while the matching thickness of the absorber is symbolized as d , and c denotes the propagation speed of the electromagnetic wave in free space.

Figure 3d illustrates the RL projection curve of the CF sample, which reveals a poor electromagnetic wave absorption performance is revealed with a RL_{\min} value of -7.93 dB at a matching thickness of 5.50 mm. The absorption performance of the CF@PPy nanocomposites is markedly enhanced with the application of a PPy shell to the CF core. As the thickness of the PPy shell increases, the absorption performance first increases but subsequently decreases, as indicated in Fig. S3. Figure S3a displays RL values versus frequency of the CP-30 nanocomposite, displaying an RL_{\min} value of -10.07 dB at a matching thickness of 2.90 mm. For the CP-60 nanocomposite (Fig. S3b), the RL_{\min} value is -13.21 dB at a matching thickness of 5.50 mm, and the optimal EAB value is 1.12 GHz. Figure 3e illustrates the performance of the CP-90 nanocomposite with a RL_{\min} value of -27.98 dB at a matching thickness of 3.05 mm and an EAB value of 2.72 GHz at a matching thickness of 5.25 mm. Figure S3c shows RL values versus frequency of CP-120 nanocomposite, from which it can be seen that the RL_{\min} value is -13.21 dB when the matching thickness is 2.57 mm, and the optimal EAB value is 1.12 GHz when the matching thickness is 2.60 mm Fig. 3f provides a more visual comparison of the absorption performance of the various CF@PPy samples with a bar graph of the RL and EAB values. Unquestionably, the CP-90 nanocomposite outperforms the others in terms of absorption performance.

It is widely acknowledged that dipole polarization significantly contributes to the dielectric loss absorbing material, which can be explained by the Debye relaxation phenomenon. The relaxation process of electromagnetic wave

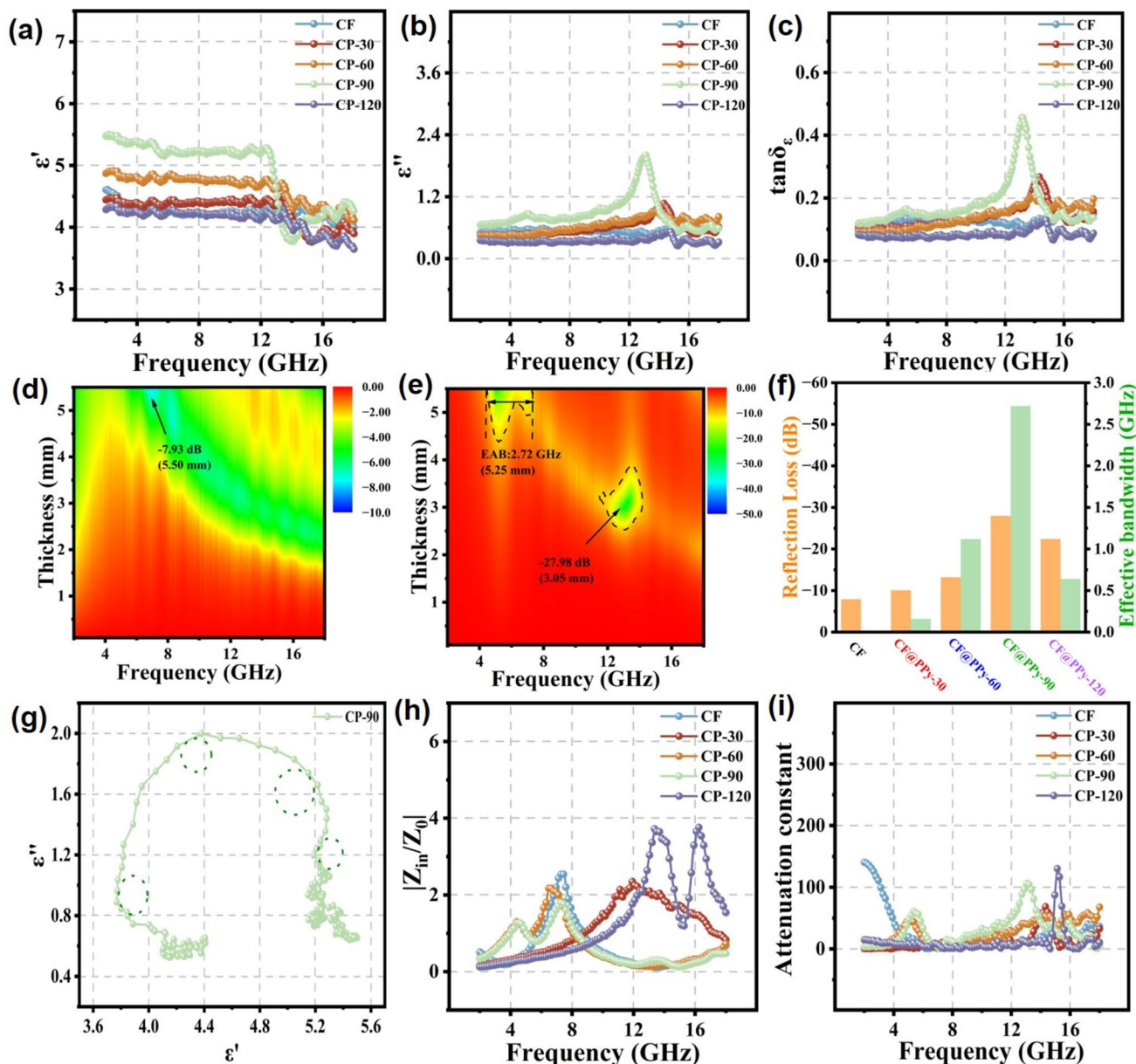


Fig. 3 **a** Real part of complex permittivity, **b** Imaginary part of complex permittivity, **c** $\tan\delta_\epsilon$ of CF, CP-30, CP -60, CP -90, CP -120; **d** RL values versus frequency of CF; **e** RL values versus frequency

of CP -90; **f** Comparison plots of RL and EAB; **g** Cole-Cole curve of CP -90; **h** $|Z_{in}/Z_0|$ of CP -90; **i** Attenuation constant of CF, CP -30, CP -60, CP -90, CP -120

absorbing materials can be represented by the following equation:

$$\left(\epsilon' - \frac{(\epsilon_s + \epsilon_\infty)}{2} \right)^2 + (\epsilon'')^2 = \left(\frac{\epsilon_s - \epsilon_\infty}{2} \right)^2 \tag{3}$$

herein, ϵ_s and ϵ_∞ represent the static and high-frequency optical permittivity, respectively. According to above equation, the relationship between ϵ' and ϵ'' should form a semicircle, and each semicircle corresponds to a Debye relaxation

process. As illustrated in Figs. 3g and S4, several semicircles can be identified in both the CF and CF@PPy samples, indicating the presence of multiple dielectric relaxations. The CP-90 nanocomposites display more semicircles, which may stem from the interfacial polarization instigated by the hetero-interfaces between CF and PPy, as well as from the inherent dipole polarization of the absorber, suggesting its good electromagnetic wave absorption capacity.

It is universally acknowledged that the impedance matching and attenuation coefficient are crucial when evaluating

the efficiency of an absorber designed for electromagnetic wave absorption. An optimal absorber should permit the maximum penetration of electromagnetic waves, necessitating effective impedance matching, which is typically evaluated using the delta function, as delineated in the following formula:

$$|\Delta| = \left| \sinh^2(kfd) - M \right| \quad (4)$$

in which, the values of K and M can be determined by the relationship between complex permittivity and complex permeability, as expressed in the following equation.

$$K = \frac{4\pi \sqrt{\mu_r \epsilon_r} \sin\left(\frac{\delta_e + \delta_m}{2}\right)}{c \cos\delta_e \cos\delta_m} \quad (5)$$

$$M = \frac{4\mu' \cos\delta_e \epsilon' \cos\delta_m}{(\mu' \cos\delta_e - \epsilon' \cos\delta_m)^2 + [\tan\left(\frac{\delta_m - \delta_e}{2}\right)]^2 (\mu' \cos\delta_e + \epsilon' \cos\delta_m)^2} \quad (6)$$

In general, a material possesses optimal impedance matching when the $|\Delta|$ value tends to zero. When the $|\Delta|$ value is less than 0.4, it can be considered that the material exhibits effective impedance matching. Figures 3h and S10 illustrate the impedance matching and $|\Delta|$ values of various CF@PPy nanocomposites under their optimal conditions, respectively. It can be observed that the CP-90 nanocomposite exhibits a larger mapping area ($|\Delta| < 0.4$) compared to other materials. These findings indicate that CP-90 nanocomposites demonstrate optimal impedance matching, enabling a higher penetration of incident electromagnetic waves into the absorber. The attenuation coefficient is used to assess the dissipation ability of incident electromagnetic waves within the absorbing material. When an absorber exhibits good impedance matching, it is necessary to maximize the dissipation of the incident electromagnetic waves to achieve effective electromagnetic wave absorption. This can be quantified using the following equation.

$$\alpha = \frac{\sqrt{2}\pi f}{c} \sqrt{(\mu''\epsilon'' - \mu'\epsilon') + \sqrt{(\mu''\epsilon'' - \mu'\epsilon')^2 + (\mu'\epsilon'' + \mu''\epsilon')^2}} \quad (7)$$

As depicted in Fig. 3i, the CF@PPy nanocomposite exhibits a significantly higher attenuation coefficient α compared to the CF sample. Notably, CP-90 demonstrates the highest α value (especially in Ku band), indicating its superior capability to dissipate electromagnetic waves energy. These findings highlight the importance of synergistically considering both impedance matching and attenuation capability to achieve outstanding microwave absorption performance. Therefore, it can be observed that the incorporation of the conductive polymer PPy effectively enhances the

impedance matching and electromagnetic wave loss capability of CF sample.

To induce magnetic loss within the CF@PPy nanocomposite, CoFe₂O₄ magnetic nanoparticles are fabricated using CF@PPy as substrate, resulting in the construction of multi-layer heterogeneous CF@PPy@CoFe₂O₄ nanocomposite. As illustrated in Fig. 4a, b, the CoFe₂O₄ nanoparticles have been successfully dispersed across the surface of the CF@PPy nanocomposites without any discernible agglomeration. The diameter of the CF@PPy@CoFe₂O₄ nanocomposite is approximately 18 μ m, larger than CF@PPy nanocomposites. The typical XRD spectrum analysis of CF@PPy@CoFe₂O₄ is presented in Fig. 4c. The broad diffraction peak observed near 26° is attributed to the presence of CF and PPy. Moreover, other distinct diffraction peaks located at 30.08°, 35.50°, 43.05°, 56.98°, and 65.68° correspond to the (220), (311), (400), (511), and (440) crystallographic facets of the CoFe₂O₄ phase (JCPDS No 22-1086) [46], thereby verifies the successful preparation of CoFe₂O₄ nanoparticles. As PPy and CoFe₂O₄ were coated on the CF surface step by step, and the CF had good stability under the given reaction conditions, the mass of CF would keep remain unchanged before and after the reaction [47, 48]. To obtain the actual content of CF and PPy in the CF@PPy@CoFe₂O₄ nanocomposite, we compared the mass changes of the products before and after the reaction and designed several contrast experiments. The actual mass fractions of various components were obtained, as shown in Table S1. The employed CF sample was 0.055 g. After being coated with the PPy layer, its mass increased to 0.092 g. The final mass of the obtained CF@PPy@CoFe₂O₄ nanocomposite was 0.104 g. Therefore, it can be calculated that the mass fraction of CF in the product is approximately 53.9 wt%, and the mass fraction of PPy in the product is approximately 34.6 wt%. To further investigate the thermal stability and decomposition behavior of the CF@PPy@CoFe₂O₄ nanocomposite, thermogravimetric analysis (TG) coupled with differential scanning calorimetry (DSC) measurements were conducted [9]. The TG-DSC curves are presented in Fig. S6. Within the test temperature range, the mass change of the product can be roughly divided into three distinct stages. In the first stage, from room temperature to 120 °C, a mass loss of 3.59% was observed, which can be attributed to the decomposition of physically adsorbed water and the removal of functional groups on the surface of the sample. The second stage, from 120 to 840 °C, exhibited a significant mass loss of 32.16%, corresponding to the decomposition of PPy. This value is in good agreement with the calculated mass fraction of PPy in the nanocomposites (Table S1). During this stage, the decomposition of PPy involves the evolution of various small-molecule substances, such as water, carbon monoxide, carbon dioxide, and ammonium chloride, in the

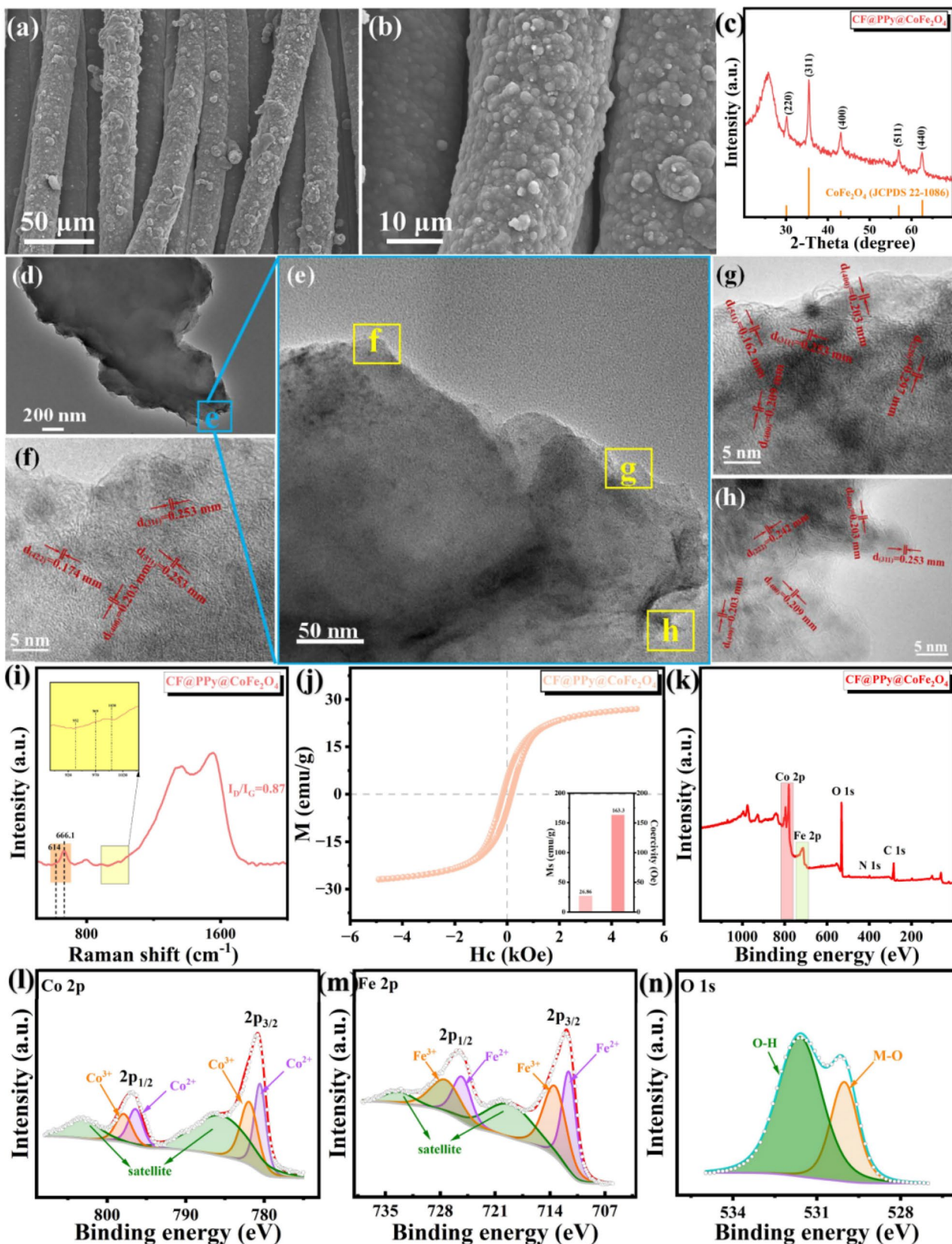


Fig. 4 a, b SEM images, c XRD pattern, d, e Typical TEM images and f–h HRTEM images of CoFe_2O_4 coating capture from CF@PPy@ CoFe_2O_4 , i Raman spectra, j hysteresis loop, XPS spectra k full scan, l Co 2p, m Fe 2p, n O 1s of CF@PPy@ CoFe_2O_4

form of gas. The third stage, above 840 °C, showed a relatively slow and steady mass loss, which can be ascribed to the gradual decomposition of CoFe_2O_4 and the remaining carbon residue. It is important to note that the mass loss observed in the third stage does not solely correspond to the decomposition of CoFe_2O_4 . Therefore, the value of 1.43% reported in the previous version of the manuscript does not accurately represent the CoFe_2O_4 content in the nanocomposites. Figure S7a illustrates typical type IV nitrogen adsorption-desorption isotherms of the $\text{CF@PPy@CoFe}_2\text{O}_4$ nanocomposites in the relative pressure (P/P_0) range of 0.5 ~ 1.0. The BET specific surface area of the sample is evaluated to be around 56.59 m^2/g , which is larger than that of the employed commercial CF carrier (about 1.31 m^2/g , provided by the manufacturer). Figure S7b shows the pore size and their distribution obtained from the adsorption branch by the Barrett-Joyner-Halenda (BJH) method, demonstrating that the pore diameter is 3.818 nm.

Systematic characterization results revealed that the CF carrier used in the experiment and the electrodeposited PPy coating are amorphous, while the CoFe_2O_4 synthesized via the hydrothermal method is crystalline. To further investigate the microstructure of the product, TEM characterization was performed. Figure 4d shows a representative image of the product, with a size of several microns, corresponding to the micro protrusions observed on the fiber surface in Fig. 4b. Figure 4e shows a magnified view of the region marked by the light blue block in Fig. 4d, revealing distinct contrast differences. Figure 4f–h are high-resolution TEM images taken from the corresponding areas in Fig. 4e, respectively. Numerous nanoscale crystal particles are randomly distributed on the product surface, exhibiting clearly visible lattice stripes. Their lattice stripes are clearly visible, and the interplanar crystal spacing corresponds to the (220), (311), (222), (400), (422), (511) planes of cobalt ferrite, respectively.

Additionally, to determine the physical phase composition of the composites, Raman and FT-IR analyses were conducted. The Raman energy spectrum of the $\text{CF@PPy@CoFe}_2\text{O}_4$ nanocomposite is displayed in Fig. 4i. The D and G bands are discernible around 1350 cm^{-1} and 1554 cm^{-1} , respectively. The I_D/I_G ratio value increases to 0.87, indicating the presence of more defect in the CF and polypyrrole due to the introduction of CoFe_2O_4 nanoparticles. Significantly, the characteristic peaks of PPy remain visible in the magnified image (highlighted in yellow). Additionally, the peaks at 614 cm^{-1} and 661 cm^{-1} are associated with the T_{1g}^{-1} and A_{1g}^{-1} vibrational modes of the CoFe_2O_4 phase respectively. Figure S8 depicts the FT-IR spectra of the $\text{CF@PPy@CoFe}_2\text{O}_4$ nanocomposite [49]. No new distinctive peaks emerge when compared with CF@PPy , signifying that the PPy continues to be encapsulated on the CF and that the integration of CoFe_2O_4 nanoparticles has

not compromised its structural integrity. The magnetization capacity of the $\text{CF@PPy@CoFe}_2\text{O}_4$ nanocomposite is characterized by room-temperature hysteresis loops [50], as depicted in Fig. 4j. The saturation magnetization intensity is 26.86 emu/g, while the remanent magnetization intensity (M_r) stands at 4.76 emu/g, as seen in the magnified image. The coercivity (H_c) is measured at 163.3 Oe, denoting the ferromagnetic nature of the CoFe_2O_4 nanoparticles. This magnetic attribute permits the composite to exhibit magnetic loss contribution, thus enhancing its impedance matching potential and loss capacity.

Figures 4k and S9 presents the XPS full scan of the $\text{CF@PPy@CoFe}_2\text{O}_4$ nanocomposite, with the emergence of characteristic peaks associated with the elements Fe and Co, signifying the successful incorporation of CoFe_2O_4 nanoparticles into CF@PPy [51]. Figure 4l illustrates the Gaussian-fitted Co 2p spectrum, comprising two primary peaks aligned with the Co 2p_{1/2} and Co 2p_{3/2} energy levels, supplemented by two vibrational satellite peaks. The binding energies of the primary Co 2p_{3/2} peaks are observed at 780.5 eV and 781.6 eV, while the peak at 796.4 eV/781.9 eV corresponds to Co 2p_{1/2}, indicating the existence of two distinct valence states of Co. The peaks at 785.7 eV and 803.2 eV are vibrational peaks originating from the coupling of the d-electron orbitals of Co atoms with spin orbita. In the Fe 2p spectrum (Fig. 4m), four main peaks are observed, with additional vibrational satellite peaks at 719.5 eV and 733.7 eV. The peaks situated at 713.7 eV and 727.5 eV mainly derive from Fe^{3+} in the tetrahedral sites, while the peaks at 711.6 eV and 723.6 eV are mainly contributed by Fe^{2+} in the octahedral sites, indicating the presence of two distinct valence states of the Fe elements. Figure 4n depicts the O 1s spectrum, which can be deconvoluted into two distinctive peaks. The peak located at 530.6 eV corresponds to the M-O bond, typical of CoFe_2O_4 (Co single bond O single bond Fe), while the peak at approximately 531.8 eV can be attributed to the O-H bond, originating from surface oxygenated functional groups and adsorbed water molecules [52].

In order to further elucidate the role of CoFe_2O_4 magnetic nanoparticles, the electromagnetic parameters of the $\text{CF@PPy@CoFe}_2\text{O}_4$ nanocomposite were examined, as illustrated in Fig. 5a–c. In Fig. 5a, a decrease ϵ' values of the $\text{CF@PPy@CoFe}_2\text{O}_4$ nanocomposite is observed with increasing frequency. This trend aligns with the frequency dispersion behavior, mainly attributed to the delayed response rate of dipole polarization to the rapidly alternating electromagnetic field. This emergence of frequency dispersion behavior enables a broader absorption band of incident electromagnetic waves. The enhanced ϵ' value of $\text{CF@PPy@CoFe}_2\text{O}_4$ nanocomposite may be ascribed to the incorporation of magnetic CoFe_2O_4 nanoparticles, which creates a greater number of heterogeneous interfaces between the three materials, thereby prompting

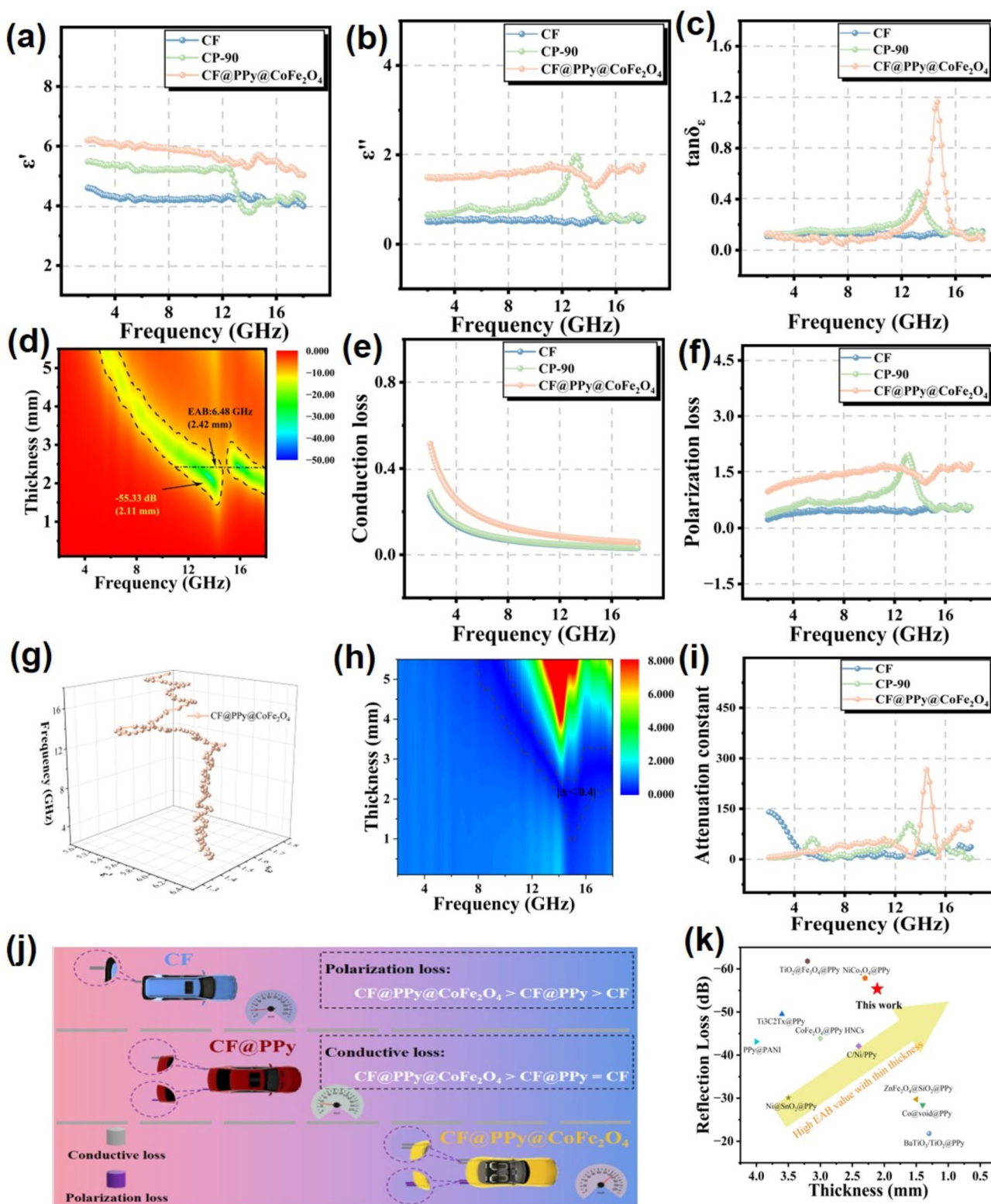


Fig. 5 **a** Real part of complex permittivity, **b** imaginary part of complex permittivity, **c** $\tan\delta_e$ of CF, CF@PPy and CF@PPy@CoFe₂O₄; **d** RL values versus frequency; **e** conduction loss and **f** polarization loss of CF, CF@PPy and CF@PPy@CoFe₂O₄; **g** Cole-Cole curve of CF@PPy@CoFe₂O₄; **h** impedance matching of CF@PPy@CoFe₂O₄;

i attenuation constant of CF,CF@PPy and CF@PPy@CoFe₂O₄; **j** schematic illustration of conductive loss and polarization loss of CF, CF@PPy and CF@PPy@CoFe₂O₄ samples; **k** RL_{min} versus thickness of microwave absorbing materials reported recently

stronger interfacial polarization and distinct polarization relaxation phenomena. Figure 5b presents the variation curves of ϵ'' values with frequency for the three materials. Notably, the CF@PPy@CoFe₂O₄ nanocomposite displays significantly higher values than the other two samples, suggesting its superior microwave absorption properties. The existence of resonance peaks in the high-frequency range also indicates the occurrence of more polarization phenomena. As depicted in Fig. 5c, the CF@PPy@CoFe₂O₄ nanocomposite exhibits an enhanced capacity for dielectric loss, particularly within the Ku band. Figure S10a illustrates the variation of μ' and μ'' values with the varying frequency of the CF@PPy@CoFe₂O₄ nanocomposite. The μ' values range from 0.8 to 1.2, while μ'' values span from 0 to 0.8. Notably, the complex permeability exhibits resonance peaks in 12 ~ 16 GHz, indicating its effective attenuation of incident microwave energy magnetic field. Generally, magnetic loss tangent ($\tan\delta_\mu$), a measure of a material's magnetic loss ability, is characterized by higher values indicating greater dissipation of magnetic field energy. The $\tan\delta_\mu$ curve of the CF@PPy@CoFe₂O₄ nanocomposite (Fig. S10b) mirrors the trend observed in the imaginary part of the permeability (as shown in Fig. S10a). Notably, in the range of 2 ~ 18 GHz, the dielectric loss tangent values overshadow those of the magnetic loss tangent, suggesting that the dielectric loss mechanism plays a dominant role in the attenuation of electromagnetic waves. Figure S10c presents the C_0 curve for the CF@PPy@CoFe₂O₄ nanocomposite. The C_0 value remains low, while in the 2 ~ 7 GHz range, it gradually decreases, indicating that magnetic loss is primarily caused by natural ferromagnetic resonance. Additionally, slight fluctuations in C_0 values in the 12 ~ 16 GHz range suggest magnetic losses due to exchange resonance. Figure 5d presents the RL projection drawing of the CF@PPy@CoFe₂O₄ nanocomposite, shows their exceptional microwave absorption properties. Notably, the RL_{\min} reaches -55.33 dB at a matching thickness of 2.11 mm, indicating efficient absorption of electromagnetic waves. Furthermore, the EAB spans a broad range of 6.48 GHz at an optimal thickness of 2.42 mm, demonstrating the material's wide absorption band. Figure S11 shows RL-frequency curves, and the relationship between the simulated thickness and the peak frequency for the samples. The quarter-wavelength formula is shown below:

$$t_m = \frac{n\lambda}{4} = \frac{nc}{4f_m \sqrt{|\mu_r| |\epsilon_r|}} \quad (n = 1, 3, 5 \dots \dots) \quad (8)$$

where t_m is the matching thickness of the absorber, λ is the wavelength of the incident electromagnetic wave, c represents the speed of light in vacuum, and f_m is the corresponding matching frequency. It can be clearly seen that the

vertical line of the RL_{\min} peak of the CF@PPy@CoFe₂O₄ nanocomposite is on the $1/4\lambda$ curve at the corresponding matching thickness.

To further analyze the dominant role of the loss mechanism in dielectric loss, ϵ'' can be divided into two parts, as represented by the following equations:

$$\epsilon'' = \epsilon_p'' + \epsilon_c'' = (\epsilon_s - \epsilon_\infty) \frac{2\pi f \tau}{1 + (2\pi f)^2 \tau^2} + \frac{\sigma}{2\pi f \epsilon_0} \quad (9)$$

where σ denotes the conductivity of the absorbing material, ϵ_p'' and ϵ_c'' represent the polarization loss and conductive loss of the absorber, respectively. The values of ϵ_p'' and ϵ_c'' are obtained using the nonlinear least-squares method of fitting. Typically, ϵ_c'' can be equated to the parallel circuit of resistance and capacitance, while ϵ_p'' represents the series circuit of resistance and capacitance. Since both CF and PPy are dielectric absorbing materials, the main loss mechanism is dielectric loss. Furthermore, the introduction of CoFe₂O₄ magnetic nanoparticles plays a role in optimizing the impedance matching as well as providing a certain amount of magnetic loss. The contribution of the CF@PPy@CoFe₂O₄ nanocomposite to the loss mechanism, including polarization loss and conductive loss, was analyzed and fitted, and the results are depicted in Fig. 5e, f. As revealed in Fig. 5e, the conductive loss curves of all three samples exhibit a gradual decrease with the increasing frequency. The polarization loss of CF@PPy@CoFe₂O₄ nanocomposite is about 1.5 in the high frequency region. Furthermore, the polarization loss curves of the three samples show similar variations to the imaginary part of the complex permittivity, displaying several resonance peaks at high frequency (Fig. 5b). Figure S12 reveals that the polarization loss ratio of the sample is greater than 0.5, indicating that the polarization loss is the dominant factor in the dielectric loss. However, it is crucial to realize that neither of these loss mechanisms can be ignored over the entire range of measured frequencies. In contrast, dielectric loss is the result of the combined action of conductive loss and polarization loss. The dielectric relaxation phenomenon of CF@PPy@CoFe₂O₄ nanocomposite is investigated using Cole-Cole semicircular curves, as shown in Fig. 5g. The appearance of semicircles indicates the occurrence of Debye relaxation phenomenon, which positively affects the dielectric relaxation of the absorber. Furthermore, the linear tails observed in the Cole-Cole curves suggest that the dominant loss mechanism in the material is conductive loss in the low-frequency range. Furthermore, the $|\Delta|$ value of the CF@PPy@CoFe₂O₄ nanocomposite (Fig. 5h) indicates a significantly larger area ($|\Delta| < 0.4$) compared to the other two reference samples, CF and CF@PPy, suggesting that the introduction of CoFe₂O₄ magnetic nanoparticles greatly enhances the impedance matching, enabling more efficient

penetration of electromagnetic waves into the interior of the absorbing material. In Fig. 5i, it can be observed that the attenuation coefficient of the CF@PPy@CoFe₂O₄ nanocomposite is higher compared to the other two samples. It suggests that the incident electromagnetic wave can be absorbed to a greater extent after entering the interior of the material.

To gain a deeper understanding of the loss mechanisms of the three materials, a comprehensive comparison of their respective conduction and polarization losses was undertaken, as illustrated in Fig. 5j. It becomes apparent that the integration of PPy shells and CoFe₂O₄ nanoparticles into the CF matrix creates multiple heterogeneous interfaces, leading to interfacial polarization. Furthermore, these diverse interfaces give rise to a multiple of dipoles that act as polarization centers, facilitating effective absorption of incident electromagnetic waves. Additionally, the introduction of magnetic CoFe₂O₄ nanoparticles not only enhances the polarization loss but also enriches the magnetic loss mechanisms of the nanocomposite. Consequently, the superior electromagnetic wave absorption capacity of CF@PPy@CoFe₂O₄ nanocomposite is governed by the combined effect of conductive loss in the low frequency range and the polarization loss in the high frequency range. In Fig. 5k, we present a comprehensive comparison of the electromagnetic wave absorption properties of the CF@PPy@CoFe₂O₄ nanocomposite with those of recently reported similar nanocomposites containing conductive polymers, and magnetic particle components [26, 29, 33, 53–59]. Notably, the CF@PPy@CoFe₂O₄ nanocomposite stands out with its broader EAB and superior RL_{min} compared to the other materials.

These remarkable findings highlight the exceptional electromagnetic wave absorption performance of the CF@PPy@CoFe₂O₄ nanocomposite, making it a highly promising candidate for applications demanding thin, wide band, lightweight, and mechanically robust absorbers.

Figure 6 exhibits the electromagnetic loss mechanism diagram of the CF@PPy@CoFe₂O₄ nanocomposite, and its outstanding microwave absorption properties can be summarized to the following reasons. Firstly, the highly conductive CF constructs a 3D conductive network, providing efficient pathways for electrons hopping and migration, thereby amplifying the conduction loss of the sample. Additionally, the 3D conductive network triggers a multiple scattering effect, generating several reflections and scattering for the incident electromagnetic wave reaching the absorber surface. Secondly, during the fabrication process of CF@PPy@CoFe₂O₄ nanocomposite, an abundance of defects and surface functional groups are introduced, resulting in the congregation of dipoles within the product. Influenced by the alternating electromagnetic field, the motion of these dipoles cannot keep up with the periodic changes of the electromagnetic wave, leading to the polarization dissipation of the electromagnetic wave. Additionally, the CoFe₂O₄ nanoparticles within the nanocomposites present eddy current effects and natural resonance, contributing to the magnetic loss capability of the sample and enriching its microwave absorption performance. Finally, the core-shell structure of CF@PPy@CoFe₂O₄ nanocomposite leads to multiple heterogeneous structures, inducing interfacial polarization phenomena, further enhancing the electromagnetic attenuation capability of the material. In conclusion, these results provide an in-depth exploration of the electromagnetic wave attenuation mechanism of the CF@PPy@CoFe₂O₄ nanocomposite and highlight the reasons behind their superior microwave absorption properties.

4 Conclusions

In this study, a core-shell heterogeneous structure by integrating a dielectric CF core, a conductive polymer PPy interlayer, and magnetic CoFe₂O₄ nanoparticles have been innovatively developed via electrodeposition and hydrothermal methodologies. The synthesized CF@PPy@CoFe₂O₄ nanocomposite displays excellent electromagnetic wave attenuation ability and optimal impedance matching properties, which can be attributed to the synergistic interplay of the various components. Notably, at a matching thickness of 2.11 mm, the nanocomposite attains a RL_{min} of -55.33 dB and an EAB value of 6.48 GHz at a matching thickness of 2.42 mm, covering the entire Ku-band. This superior performance is credited to multiple loss mechanisms, including

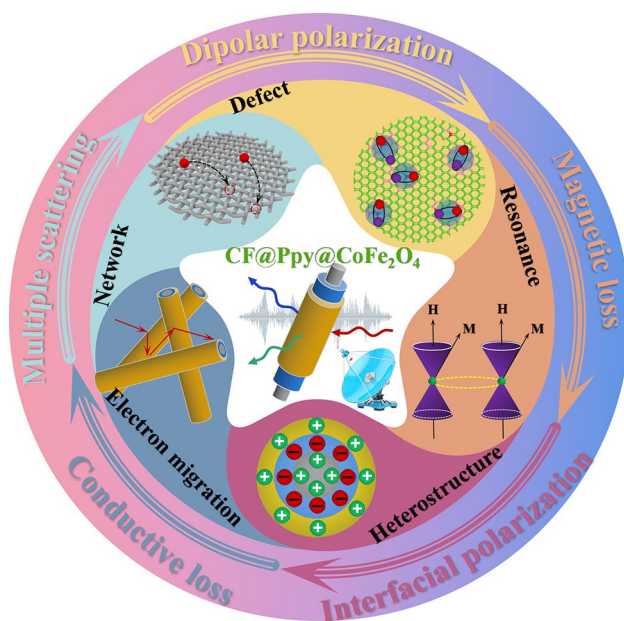


Fig. 6 Schematic diagrams of electromagnetic wave attenuation approaches of CF@PPy@CoFe₂O₄ nanocomposite

conduction loss, interfacial/dipole polarization, and natural resonance, which interact with each other and contribute to the electromagnetic wave attenuation of the absorber. Importantly, the introduction of the conductive polymer PPy enhances the impedance matching of the sample, while the employment of CoFe_2O_4 nanoparticles enriches the magnetic loss mechanisms. In conclusion, the $\text{CF@PPy@CoFe}_2\text{O}_4$ nanocomposite provides significant insights into the microwave absorption mechanism of core-shell structured nanocomposites and serve as a robust foundation for future investigations in this arena.

Supplementary Information The online version contains supplementary material available at <https://doi.org/10.1007/s42114-024-00864-z>.

Author contributions Yuan: Conceptualization, Validation, Formal analysis, Investigation, Data curation, Writing-original draft, Writing-review & editing. Zhao: Conceptualization, Validation, Formal analysis. Miao: Methodology, Formal analysis, Investigation, Data curation, Writing-review & editing. Wang: Methodology, Investigation. Cui: Formal analysis, Investigation. Tian: Formal analysis, Investigation. Wang: Investigation, Data curation. Zhang: Conceptualization, Methodology, Validation, Formal analysis, Investigation, Data curation, Writing-original draft, Writing-review & editing, Visualization. Li: Investigation, Formal analysis, Data curation, Supervision. Meng: Conceptualization, Validation, Formal analysis, Data curation, Writing - original draft, Writing-review & editing, Supervision.

Funding The work reported here was supported by the National Natural Science Foundation of China under Grant No. 52072196, 52002200, 52102106, 52202262, 22379081, 22379080, Major Basic Research Program of Natural Science Foundation of Shandong Province under Grant No. ZR2020ZD09, the Natural Science Foundation of Shandong Province under Grant No. ZR2020QE063, ZR2022ME090, ZR2023QE059. Moreover, this work was supported by the Visiting Scholar Fellowship Funding for Teachers in Shandong Province's General Undergraduate Institutions.

Data availability The data will be available upon proper request.

Declarations

Competing interests The authors declare no competing interests.

References

- Li F, Wu N, Kimura H et al (2023) Initiating binary metal oxides microcubes electromagnetic wave absorber toward ultra-broad absorption bandwidth through interfacial and defects modulation. *Nanomicro Lett* 15(1):220. <https://doi.org/10.1007/s40820-023-01197-0>
- Kim S, Lee S, Zhang Y et al (2023) Carbon-based radar absorbing materials toward stealth technologies. *Adv Sci* 10(32):2303104. <https://doi.org/10.1002/advs.202303104>
- Zhang Y, Gao S, Xia B et al (2023) Coal gasification fine slag doped with Fe_3O_4 : high-performance electromagnetic-wave absorbers. *J Magn Mater* 580:170916. <https://doi.org/10.1016/j.jmmm.2023.170916>
- Wu Y, Chen L, Han Y et al (2023) Hierarchical construction of CNT networks in aramid papers for high-efficiency microwave absorption. *Nano Res* 16:7801–7809. <https://doi.org/10.1007/s12274-023-5522-4>
- Gu H, Huang J, Li N et al (2023) Reactive MnO_2 template-assisted synthesis of double-shelled PPy hollow nanotubes to boost microwave absorption. *J Mater Sci Technol* 146:145–153. <https://doi.org/10.1016/j.jmst.2022.11.010>
- Lan D, Wang Y, Wang YY et al (2023) Impact mechanisms of aggregation state regulation strategies on the microwave absorption properties of flexible polyaniline. *J Colloid Interface Sci* 651:494–503. <https://doi.org/10.1016/j.jcis.2023.08.019>
- Zheng Q, Cao WQ, Zhai H et al (2023) Tailoring carbon-based nanofiber microstructures for electromagnetic absorption, shielding, and devices. *Mater Chem Front* 7:1737–1759. <https://doi.org/10.1039/D2QM01271E>
- Wu X, Huang J, Gu H et al (2022) Ni Doping in $\text{MnO}_2/\text{MXene}$ ($\text{Ti}_3\text{C}_2\text{T}_x$) composites to modulate the Oxygen vacancies for boosting microwave absorption. *ACS Appl Electron Mater* 4(7):3694–3706. <https://doi.org/10.1021/acsaem.2c00654>
- Yang W, Peng D, Kimura H et al (2022) Honeycomb-like nitrogen-doped porous carbon decorated with Co_3O_4 nanoparticles for superior electrochemical performance pseudo-capacitive lithium storage and supercapacitors. *Adv Compos Hybrid Mater* 5:3146–3157. <https://doi.org/10.1007/s42114-022-00556-6>
- Gao S, Zhang Y, Zhang X et al (2023) Synthesis of hollow ZnFe_2O_4 /residual carbon from coal gasification fine slag composites for multiband electromagnetic wave absorption. *J Alloys Compd* 952:170016. <https://doi.org/10.1016/j.jallcom.2023.170016>
- She L, Zhao B, Yuan M et al (2022) Joule-heated flexible carbon composite towards the boosted electromagnetic wave shielding properties. *Adv Compos Hybrid Mater* 5(4):3012–3022. <https://doi.org/10.1007/s42114-022-00530-2>
- Guo Y, Ruan K, Wang G et al (2023) Advances and mechanisms in polymer composites toward thermal conduction and electromagnetic wave absorption. *Sci Bull* 68:1195–1212. <https://doi.org/10.1016/j.scib.2023.04.036>
- Wang L, Li X, Li Q et al (2019) Oriented polarization tuning Broadband absorption from flexible hierarchical ZnO arrays vertically supported on carbon cloth. *Small* 15:1900900. <https://doi.org/10.1002/sml.201900900>
- Wang J, Liu L, Jiao S et al (2020) Hierarchical carbon fiber@MXene@ MoS_2 core-sheath synergistic microstructure for tunable and efficient microwave absorption. *Adv Funct Mater* 30:2002595. <https://doi.org/10.1002/adfm.202002595>
- Zhang W, Zhang X, Zhu Q et al (2021) High-efficiency and wide-bandwidth microwave absorbers based on MoS_2 -coated carbon fiber. *J Colloid Interface Sci* 586:457–468. <https://doi.org/10.1016/j.jcis.2020.10.109>
- Yan Y, Jiang Y, Ng ELL (2023) Progress and opportunities in additive manufacturing of electrically conductive polymer composites. *Mater Today Adv* 17:100333. <https://doi.org/10.1016/j.mtadv.2022.100333>
- Hou C, Wang B, Murugadoss V et al (2020) Recent advances in Co_3O_4 as Anode materials for high-performance lithium-ion batteries. *Energy Sci Eng* 11:19–30. <https://doi.org/10.30919/es8d1128>
- Pan F, Wu X, Batalu D et al (2023) Assembling of low-dimensional aggregates with interlaminar electromagnetic synergy network for high-efficient microwave absorption. *APM* 2(2):100100. <https://doi.org/10.1016/j.apmate.2022.100100>
- Li Z, Lin H, Xie Y et al (2022) Monodispersed Co@C nanoparticles anchored on reclaimed carbon black toward high-performance electromagnetic wave absorption. *J Mater Sci Technol* 124:182–192. <https://doi.org/10.1016/j.jmst.2022.03.004>
- Guo Y, Zhang M, Cheng T et al (2023) Enhancing electromagnetic wave absorption in carbon fiber using FeS_2 nanoparticles. *Nano Res* 16:9591–9601. <https://doi.org/10.1007/s12274-023-5776-x>

21. Ruan J, Chang Z, Rong H et al (2023) High-conductivity nickel shells encapsulated wood-derived porous carbon for improved electromagnetic interference shielding. *Carbon* 213:118208. <https://doi.org/10.1016/j.carbon.2023.118208>
22. Li F, Li Q, Kimura H et al (2023) Morphology controllable urchin-shaped bimetallic nickel-cobalt oxide/carbon composites with enhanced electromagnetic wave absorption performance. *J Mater Sci Technol* 148:250–259. <https://doi.org/10.1016/j.jmst.2022.12.003>
23. Feng S, Zhai F, Su H et al (2023) Progress of metal organic frameworks-based composites in electromagnetic wave absorption. *Mater Today Phys* 30:100950. <https://doi.org/10.1016/j.mtphys.2022.100950>
24. Li F, Bi Z, Kimura H et al (2023) Energy- and cost-efficient salt-assisted synthesis of nitrogen-doped porous carbon matrix decorated with nickel nanoparticles for superior electromagnetic wave absorption. *Adv Compos Hybrid Mater* 6:133. <https://doi.org/10.1007/s42114-023-00710-8>
25. Luo F, Liu D, Cao T et al (2021) Study on broadband microwave absorbing performance of gradient porous structure. *J Alloys Compd* 4:591–601. <https://doi.org/10.1007/s42114-021-00275-4>
26. Ding J, Wang L, Zhao Y et al (2019) Boosted interfacial polarization from Multishell $\text{TiO}_2@\text{Fe}_3\text{O}_4@\text{PPy}$ Heterojunction for enhanced microwave absorption. *Small* 15:1902885. <https://doi.org/10.1002/smll.201902885>
27. Zhang M, Ling H, Ding S et al (2021) Synthesis of CF@PANI hybrid nanocomposites decorated with Fe_3O_4 nanoparticles towards excellent lightweight microwave absorber. *Carbon* 174:248–259. <https://doi.org/10.1016/j.carbon.2020.12.005>
28. Liu T, Liu N, Zhai S et al (2019) Tailor-made core/shell/shell-like $\text{Fe}_3\text{O}_4@\text{SiO}_2@\text{PPy}$ composites with prominent microwave absorption performance. *J Alloys Compd* 779:831–843. <https://doi.org/10.1016/j.jallcom.2018.11.167>
29. Wang Q, Wu X, Huang J et al (2022) Enhanced microwave absorption of biomass carbon/nickel/polypyrrole (C/Ni/PPy) ternary composites through the synergistic effects. *J Alloys Compd* 890:161887. <https://doi.org/10.1016/j.jallcom.2021.161887>
30. Badakhsh A, Han W, Jung SC et al (2019) Preparation of boron nitride-coated carbon fibers and synergistic improvement of thermal conductivity in their polypropylene-matrix composites. *Polymers* 11(12):2009. <https://doi.org/10.3390/polym11122009>
31. Chen B, Zhu Z, Ma J et al (2013) Surfactant assisted Ce-Fe mixed oxide decorated multiwalled carbon nanotubes and their arsenic adsorption performance. *J Mater Chem A* 1:11355–11367. <https://doi.org/10.1039/C3TA11827D>
32. Zhou W, Long L, Xiao P et al (2019) Comparison in dielectric and microwave absorption properties of SiC coated carbon fibers with PyC and BN interphases. *Surf Coat Technol* 359:272–277. <https://doi.org/10.1016/j.surfcoat.2018.10.104>
33. Tian C, Du Y, Xu P et al (2015) Constructing uniform core-shell PPy@PANI composites with tunable shell thickness toward enhancement in microwave absorption. *ACS Appl Mater Interfaces* 7:20090–20099. <https://doi.org/10.1021/acsami.5b05259>
34. Cheng T, Guo Y, Xie Y et al (2023) Customizing the structure and chemical composition of ultralight carbon foams for superior microwave absorption performance. *Carbon* 206:181–191. <https://doi.org/10.1016/j.carbon.2023.02.052>
35. Wang M, Peng M, Weng YX et al (2019) Toward durable and robust superhydrophobic cotton fabric through hydrothermal growth of ZnO for oil/water separation. *Cellulose* 26:8121–8133. <https://doi.org/10.1007/s10570-019-02635-2>
36. Ahmad S, Khan I, Husain A et al (2020) Electrical conductivity based ammonia sensing properties of polypyrrole/MoS₂. *Polym. Compos* 12:3047. <https://doi.org/10.3390/polym12123047>
37. Liu Z, Zhao Z, Wang Y et al (2017) In situ exfoliated, edge-rich, oxygen-functionalized graphene from carbon fibers for oxygen electrocatalysis. *Adv Mater* 29:1606207. <https://doi.org/10.1002/adma.201606207>
38. Wang L, Yang H, Liu X et al (2017) Constructing hierarchical teardrop-like $\alpha\text{-Fe}_2\text{O}_3/\text{PPy}$ nanoarrays on carbon cloth for solid-state asymmetric supercapacitors. *Angew Chem Int Ed* 56:1105–1110. <https://doi.org/10.1002/anie.201609527>
39. Ren L, Wang Y, Zhang X et al (2023) Efficient microwave absorption achieved through in situ construction of core-shell $\text{CoFe}_2\text{O}_4@\text{mesoporous carbon hollow spheres}$. *Int J Min Metall Mater* 30:504–514. <https://doi.org/10.1007/s12613-022-2509-1>
40. Tian W, Li Y, Zhou J et al (2021) Implantable and biodegradable micro-supercapacitor based on a superassembled three-dimensional network Zn@PPy hybrid electrode. *ACS Appl Mater Interfaces* 13:8285–8293. <https://doi.org/10.1021/acsami.0c19740>
41. Huyan C, Ding S, Lyu Z et al (2021) Selective removal of Perfluorobutyric Acid using an Electroactive Ion Exchanger based on Polypyrrole@Iron Oxide on Carbon Cloth. *ACS Appl Mater Interfaces* 13:48500–48507. <https://doi.org/10.1021/acsami.1c09374>
42. Liu P, Gao T, He W et al (2023) Electrospinning of hierarchical carbon fibers with multi-dimensional magnetic configurations toward prominent microwave absorption. *Carbon* 202:244–253. <https://doi.org/10.1016/j.carbon.2022.10.089>
43. Ding D, Wang Y, Li X et al (2017) Rational design of core-shell Co@C microspheres for high-performance microwave absorption. *Carbon* 111:722–732. <https://doi.org/10.1016/j.carbon.2016.10.059>
44. Zhang M, Ling H, Wang T et al (2022) An equivalent substitute strategy for constructing 3D ordered porous carbon foams and their electromagnetic attenuation mechanism. *Nano-Micro Lett* 14:157. <https://doi.org/10.1007/s40820-022-00900-x>
45. Hou C, Li F, Kimura H et al (2023) Sodium chloride assisted synthesis of porous magnetic carbon nanocomposites containing cobalt nanoparticles for high-performance electromagnetic wave-absorption. *J Mater Res Technol* 25:5148–5158. <https://doi.org/10.1016/j.jmrt.2023.07.010>
46. Hu D, Zhao F, Zhang Z et al (2018) Synthesis and magnetic properties of monodisperse CoFe_2O_4 nanoparticles coated by SiO_2 . *Ceram. Int* 44:22462–22466. <https://doi.org/10.1016/j.ceramint.2018.09.014>
47. Wang S, Liu Z, Liu Q et al (2023) Promoting the microwave absorption performance of hierarchical CF@NiO/Ni composites via phase and morphology evolution. *Int J Min* 30(3):494–503. <https://doi.org/10.1007/s12613-022-2524-2>
48. Hou C, Yang W, Kimura H et al (2023) Boosted lithium storage performance by local build-in electric field derived by oxygen vacancies in 3D holey N-doped carbon structure decorated with molybdenum dioxide. *J Mater Sci Technol* 142:185–195. <https://doi.org/10.1016/j.jmst.2022.10.007>
49. Bartůněk V, Sedmidubský D, Huber Š et al (2018) Synthesis and properties of nanosized stoichiometric cobalt ferrite spinel. *Materials* 11:1241. <https://doi.org/10.3390/ma11071241>
50. Liu X, Qin Y, Yan Y et al (2017) The fabrication of CdS/ CoFe_2O_4 /rGO photocatalysts to improve the photocatalytic degradation performance under visible light. *RSC Adv* 7:40673–40681. <https://doi.org/10.1039/C7RA07202C>
51. Zhu X, Zhao H, Niu X et al (2016) A comparative study of carbon nanotube supported MFe_2O_4 spinels (M=Fe, Co, Mn) for amperometric determination of H_2O_2 at neutral pH values. *Microchim Acta* 183:2431–2439. <https://doi.org/10.1007/s00604-016-1887-3>
52. Zhao Y, Ma X, Xu P et al (2018) Elemental mercury removal from flue gas by CoFe_2O_4 catalyzed peroxymonosulfate. *J Hazard Mater* 341:228–237. <https://doi.org/10.1016/j.jhazmat.2017.07.047>

53. Ren X, Wang J, Yin H et al (2022) Hierarchical CoFe_2O_4 @PPy hollow nanocubes with enhanced microwave absorption. *Appl Surf Sci* 575:151752. <https://doi.org/10.1016/j.apsusc.2021.151752>
54. Liu T, Liu N, An Q et al (2019) Designed construction of $\text{Ti}_3\text{C}_2\text{T}_x$ @PPY composites with enhanced microwave absorption performance. *J Alloys Compd* 802:445–457. <https://doi.org/10.1016/j.jallcom.2019.06.243>
55. Fu Y, Liao H, Wang B et al (2022) Constructing yolk-shell Co@void@PPy nanocomposites with tunable dielectric properties toward efficient microwave absorption. *J Alloys Compd* 890:161715. <https://doi.org/10.1016/j.jallcom.2019.06.243>
56. Ge Y, Li C, Waterhouse G I N et al (2021) ZnFe_2O_4 @ SiO_2 @Polypyrrole nanocomposites with efficient electromagnetic wave absorption properties in the K and Ka band regions. *Ceram Int* 47(2):1728–1739. <https://doi.org/10.1016/j.jallcom.2021.161887>
57. Wang Y, Zhang W, Luo C et al (2016) Fabrication and high-performance microwave absorption of Ni@SnO_2 @PPy Core-Shell composite. *Synth Met* 220:347–355. <https://doi.org/10.1016/j.synthmet.2016.07.005>
58. Wang R, Zhu X, Chen P et al (2023) Constructing Core-Shell NiCo_2O_4 @PPy nanocomposites with controllable dielectric properties toward wide-band microwave absorption. *J Magn Magn Mater* 580:170872. <https://doi.org/10.1016/j.jmmm.2023.170872>
59. Mao D, Zhang Z, Yang M et al (2023) Constructing $\text{BaTiO}_3/\text{TiO}_2$ @polypyrrole composites with hollow multishelled structure for enhanced electromagnetic wave absorbing properties. *Int J Min Metall Mater* 30(3):581–590. <https://doi.org/10.1007/s12613-022-2556-7>

Publisher's Note Springer Nature remains neutral with regard to jurisdictional claims in published maps and institutional affiliations.

Springer Nature or its licensor (e.g. a society or other partner) holds exclusive rights to this article under a publishing agreement with the author(s) or other rightsholder(s); author self-archiving of the accepted manuscript version of this article is solely governed by the terms of such publishing agreement and applicable law.